JOURNAL OF SPACECRAFT AND ROCKETS
Vol. 40, No. 3, May–June 2003

Prediction of Damping Coefficients Using the Unsteady Euler Equations

Soo Hyung Park,* Yoonsik Kim,* and Jang Hyuk Kwon†
Korea Advanced Institute of Science and Technology, Daejon 305-701, Republic of Korea

A prediction method for dynamic damping coefficients using the unsteady Euler equations is presented. Direct unsteady simulation can be used to compute the pitch-damping moment without any geometric approximations when compared to the steady methods using the coning motions. A forced harmonic pitching motion is employed to generate the pitch-damping moments. To compute the pitch- and the roll-damping moments for the basic finner, a dual-time stepping algorithm combined with an implicit multigrid method is applied. The computed coefficients show good agreement with the experimental data. Grid refinement and parametric studies are performed to assess the accuracy of the numerical method. The linearity of the angular rates and the variation with Mach numbers are examined for both pitch- and roll-damping moment coefficients. Through analysis of the pressure distributions at various Mach numbers, the large variations of roll-damping moment coefficient in the transonic region are explained in detail.

Nomenclature

C_l	=	rolling moment coefficient
C_{l_p}	=	roll-damping moment coefficient, $(2U_\infty/D)(\partial C_l/\partial p)$
C_m	=	pitching moment coefficient
$C_{m_q} + C_{m_{\dot\alpha}}$	=	pitch-damping moment coefficient (sum), $(2U_\infty/D)(\partial C_m/\partial \dot\alpha)$
D	=	base diameter, m
e	=	total energy, nondimensionalized by p_∞/ρ_∞
$\boldsymbol{F}$	=	inviscid flux vectors
J	=	Jacobian
k	=	reduced frequency for harmonic pitching motion, $q_o D/\alpha_o U_\infty$
L	=	multigrid level
M	=	Mach number
p	=	pressure nondimensionalized by p_∞, as used in the Euler equations; roll rate, rad/s
p^*	=	nondimensional roll rate, pD/U_∞
q	=	pitch rate, rad/s
$\boldsymbol{q}$	=	conservative flow variable vector
q_o	=	pitch rate evaluated at mean angle of attack, rad/s
$\boldsymbol{R}$	=	flux residual vector
$\boldsymbol{R}^U$	=	unsteady residual vector
T	=	nondimensional period for a cycle
$\boldsymbol{T}$	=	right eigenvector matrix
t	=	physical time, s
t^*	=	nondimensional physical time, $(t/D)\sqrt{(p_\infty/\rho_\infty)}$
U	=	freestream speed, m/s
$\boldsymbol{U}$	=	contravariant velocities
$\boldsymbol{U}_g$	=	grid velocity vector of moving grid
u, v, w	=	nondimensional velocity components in x, y, and z directions
x, y, z	=	Cartesian coordinates
α	=	angle of attack, deg
α_m	=	mean angle of attack, deg
α_o	=	amplitude of angle of attack, deg
γ	=	the ratio of specific heats
$\boldsymbol{\Lambda}$	=	diagonal matrix of eigenvalues of the Euler equations
ξ, η, ζ	=	generalized coordinates
ρ	=	density, nondimensionalized by ρ_∞
τ	=	pseudotime

Subscript

∞	=	freestream condition

Superscripts

n, m	=	time-step levels
$\cdot$	=	rate of change with respect to time

Introduction

THE ability to predict projectile flight motion is important in the body shape and controller design process.[1] The in-flight motion and static and dynamic stability are determined by the aerodynamic forces and moments that are predicted by means of experimental or numerical methods. Until now, many efforts have concentrated on the numerical prediction of the static aerodynamic coefficients, such as the drag and moment coefficients.[2] The methods for the prediction of dynamic damping coefficients, such as pitch- or roll-damping coefficients, were proposed somewhat later. Ever since Tobak et al.[3] proposed the aerodynamics of bodies of revolution in a coning motion, the steady coning motions in a noninertial rotating framework have commonly been used to predict the pitch-damping coefficients.[4–6] The roll-damping coefficients were also computed using the noninertial rotating framework.[7]

The steady methods provide a cost-effective approach for the aerodynamics associated with unsteady or time-dependent motions.[1] Deficiencies of these methods are that they require the Magnus force or moment (see Ref. 8) to be determined explicitly from other sources and that they sometimes require a geometrical constraint such as axisymmetry.[6] Full unsteady methods in the inertial coordinate frame are rarely applied to predict the dynamic damping coefficients because of the tremendously large computing time and hardware requirements. However, unsteady methods in the inertial coordinate frame enable us to compute the damping forces and moments directly, without any theoretical assumptions and geometrical constraints. This is the main reason why we have adopted an unsteady approach for finned projectiles, although it is time consuming.

Received 2 July 2001; presented as Paper 2002-0715 at the AIAA 39th Aerospace Sciences Meeting, Reno, NV, 8–11 January 2002; revision received 4 December 2002; accepted for publication 9 December 2002.

*Doctoral Candidate, Department of Aerospace Engineering.
†Professor, Department of Aerospace Engineering, 373-1 Guseong-dong, Yuseong-gu. Senior Member AIAA.

The efficiency of unsteady methods is an important factor to apply in the prediction of dynamic damping coefficients. The dual-time stepping approach[9] has led to considerable improvements compared with explicit methods based on a single time discretization. Because the marching is done in pseudotime, acceleration techniques for steady flow calculations can be used, such as local time stepping, multigrid, and implicit methods.[10] In this paper, a dual-time stepping algorithm with a multigrid diagonalized alternate directional implicit(DADI) method[11] is applied to compute the dynamic damping moments.

The basic finner model[12] has been used to validate the predicting capability of the present unsteady method. Many experimental data[12,13] and empirical theories[14] for the roll-damping coefficients showed that the coefficient C_{l_p} is inversely proportional to the Mach number, and the measured C_{l_p} is invariant with roll rate in supersonic flows. Murthy[13] measured the coefficients in the subsonic and transonic regions using the steady roll test technique. His measurement is interesting in that the measured coefficients undergo a large increase, followed by an equally large decrease at about a Mach number of 1.1.

In this study, a comparative discussion of the steady and unsteady methods is presented first. The pitch- and roll-damping moment coefficients are predicted for the basic finner configuration using the unsteady method. Grid refinement and parametric studies for the numerical method are performed. The nonlinear behaviors of roll damping in the transonic region are discussed in detail.

Theoretical Approach

The stability of projectile is described through the dynamic damping coefficients, as well as the static force and moment coefficients. The dynamic damping coefficients can be obtained by steady or unsteady flow simulations for specified motions. Previously, Tobak et al.[3] built up the nonlinear theory of bodies of revolution in coning motions and showed that the linear pitch-damping coefficients are related to the side forces and moments due to coning motions. To confirm their aerodynamic theory, Schiff[4] solved the steady Euler equations to compute the supersonic inviscid flow around the body in coning motion. The computation was based on that the flow is steady if a rotating coordinate frame is used. Schiff adopted a "lunar coning" motion to determine pitch-damping coefficients from the computed side moments. The lunar coning motion can be applied for both the axisymmetric and nonaxisymmetric bodies. This approach was employed in determining the pitch-damping coefficients for supersonic finned projectiles.[5]

The problem with the lunar coning motion[6] is that the side moment is proportional to the sum of the pitch-damping moment sum and the Magnus moment. It is possible to neglect the Magnus moment because it is small relative to the pitch-damping moment sum, especially in the supersonic flow. The lunar coning approach is thought of as an excellent engineering method in predicting the pitch-damping coefficients for finned projectiles. If the Magnus moment can not be neglected in the case of a finned projectile, it must be determined from other sources, such as experiment or direct unsteady simulation (see Ref. 8). To determine the pitch-damping moment sum directly, Weinacht et al.[6] proposed the "combined spinning and coning" motion, which allows the side moment to be proportional to the pitch-damping moment only. This motion only produces a steady flowfield for axisymmetric bodies and requires an unsteady approach for nonaxisymmetric bodies such as finned bodies.

The direct unsteady approach does not involve the approximation of ignoring the Magnus effect required by the steady lunar coning approach. Furthermore, it does not require any geometrical constraints such as axisymmetry. To describe the unsteady method for predicting the damping coefficients, the specified unsteady motions that produce damping moments should be defined. The pitch-damping moment sum can be obtained from the forced harmonic pitching motion about the c.g. in rectilinear flight. The planar pitching motion is defined by the angle of attack and pitch rate as a function of time as

$$\alpha(t^*) = \alpha_m + \alpha_o \sin\left(\sqrt{\gamma} M_\infty k t^*\right) \tag{1}$$

$$q(t^*) = \dot{\alpha}(t^*) = q_o \cos\left(\sqrt{\gamma} M_\infty k t^*\right) \tag{2}$$

In rectilinear motion, the angular rates q and $\dot{\alpha}$ are equal, and the pitch-damping coefficients can be summed and treated as a single coefficient. The moment coefficients for the pitching motion can be expanded with first-order terms for the rates, as follows:

$$C_m(t^*) = C_m|_{\alpha_m} + C_{m_\alpha} \cdot \alpha(t^*) + (D/2U_\infty)\left[C_{m_{\dot{\alpha}}} + C_{m_q}\right] \cdot \dot{\alpha}(t^*) \tag{3}$$

If α_o is small, and the variation of the pitch-damping moment coefficients' sum is small near the angle of α_m, the coefficients' sum can be determined by integrating Eq. (3):

$$C_{m_q} + C_{m_{\dot{\alpha}}}|_{q=q_o} = \left(\frac{2U_\infty}{D}\right)\frac{\int C_m \, \mathrm{d}\alpha}{\int \dot{\alpha} \, \mathrm{d}\alpha}$$

$$= \frac{2\sqrt{\gamma} M_\infty}{\pi \alpha_o} \int_0^T C_m \cos\left(\sqrt{\gamma} M_\infty k t^*\right) \mathrm{d}t^* \tag{4}$$

The roll-damping coefficients can be obtained easily because the pure rolling motion is described by a constant roll rate p^*:

$$C_{l_p} = 2\frac{\partial C_l}{\partial p^*} \tag{5}$$

This rolling motion of the body in the inertial framework is identical to the rotation of the body axis in the noninertial framework. In the latter case, the governing equations are modified to include the noninertial terms such as the Coriolis and centrifugal force terms.[7]

Numerical Methods

Governing Equations

In this paper, the following integral form of the three-dimensional compressible Euler equations is considered over a control volume $\mathcal{V}(t)$:

$$\frac{\mathrm{d}}{\mathrm{d}t}\int_{\mathcal{V}(t)} \boldsymbol{q} \, \mathrm{d}\mathcal{V} + \int_{\partial\mathcal{V}(t)} \boldsymbol{F} \, \mathrm{d}\mathcal{S} = 0 \tag{6}$$

with

$$\boldsymbol{q} = [\rho, \rho u, \rho v, \rho w, \rho e]^T \tag{7}$$

$$\boldsymbol{F} = \begin{bmatrix} \rho \boldsymbol{U} \\ \rho u \boldsymbol{U} + n_x p \\ \rho v \boldsymbol{U} + n_y p \\ \rho w \boldsymbol{U} + n_z p \\ (\rho e + p)\boldsymbol{U} + p \boldsymbol{U}_g \end{bmatrix} \tag{8}$$

where $\boldsymbol{U}$ means the relative flow velocity at the control surfaces in each direction:

$$\boldsymbol{U} = n_x u + n_y v + n_z w - \boldsymbol{U}_g \tag{9}$$

Equation (6) can be discretized with the cell-centered finite volume method and integrated cellwise in the computational space domain. To compute the residual over each cell, the Roe scheme is used, and a second-order upwind total variational diminishing scheme with a minmod limiter is adopted to improve the solution accuracy.[15]

Multigrid DADI Method

Dual-time stepping[9] with a DADI method is used to advance the solution in time. This allows one not only to use a large time increment, but to maintain temporal accuracy. The dual-time stepping also eliminates factorization and linearization errors by iterating the solutions along a pseudotime. The time derivative for the physical time is approximated by assuming that the backward difference discretization is second order, and so the governing equations become

$$\boldsymbol{R}^U_{ijk} = \frac{3\boldsymbol{q}^{n+1}_{ijk} - 4\boldsymbol{q}^{n}_{ijk} + \boldsymbol{q}^{n-1}_{ijk}}{2J\Delta t^*} + \boldsymbol{R}^{n+1}_{ijk} = 0 \tag{10}$$

Here, it is convenient to define a new residual $\boldsymbol{R}^U$. Equation (10) can be considered the equation of the steady-state problem by introducing a derivative with respect to a pseudotime τ:

$$\frac{\mathrm{d}\boldsymbol{Q}_{ijk}^{m+1}}{J\,\mathrm{d}\tau} + \boldsymbol{R}_{ijk}^{U} = 0 \tag{11}$$

The steady-state solution of Eq. (11) that satisfies $\boldsymbol{R}_{ijk}^{U} = 0$ is the solution of the unsteady equations.

The pseudotime problem can be solved by using any of the time-marching methods that have been proposed to solve steady-state problems, as well as any of the convergence acceleration techniques.[9] In this work, the DADI method[11] is used to find steady-state solutions. An implicit pseudotime stepping method[10] can be written as

$$\left[\left(\frac{1}{J\Delta\tau} + \frac{3}{2J\Delta t^*}\right)\boldsymbol{I} + \frac{\partial \boldsymbol{R}}{\partial \boldsymbol{q}}\right]\Delta\boldsymbol{q} = -\boldsymbol{R}_{ijk}^{U}(\boldsymbol{q}^m) \tag{12}$$

When an alternate directional implicit (ADI) method is used, Eq. (12) can be factorized as follows:

$$\{\boldsymbol{D} + \boldsymbol{A}_\xi\}\boldsymbol{D}^{-1}\{\boldsymbol{D} + \boldsymbol{A}_\eta\}\boldsymbol{D}^{-1}\{\boldsymbol{D} + \boldsymbol{A}_\zeta\}\Delta\boldsymbol{q} = -\boldsymbol{R}^U \tag{13}$$

where

$$\boldsymbol{D} = \left(\frac{1}{J\Delta\tau} + \frac{3}{2J\Delta t^*}\right)\boldsymbol{I} \tag{14}$$

Here, $\boldsymbol{A}_i = (\partial \boldsymbol{R}/\partial \boldsymbol{q})$ in each direction are the Jacobian matrices of a residual that differs according to the spatial discretization method.[11] Finally, Eq. (13) can be expressed in a DADI form by using the similarity transformation[16]

$$\boldsymbol{T}_\xi\{\boldsymbol{D} + \boldsymbol{\Lambda}_\xi\}\boldsymbol{T}_\xi^{-1}\boldsymbol{D}^{-1} \times \boldsymbol{T}_\eta\{\boldsymbol{D} + \boldsymbol{\Lambda}_\eta\}\boldsymbol{T}_\eta^{-1}\boldsymbol{D}^{-1}$$

$$\times \boldsymbol{T}_\zeta\{\boldsymbol{D} + \boldsymbol{\Lambda}_\zeta\}\boldsymbol{T}_\zeta^{-1}\Delta\boldsymbol{q} = -\boldsymbol{R}^U \tag{15}$$

The use of an efficient multigrid algorithm reduces the number of pseudotime iterations, as well as the computing time of the steady initial solutions. To implement the multigrid on the DADI method with the dual-time stepping method, some modifications are applied to the standard sawtooth cycle algorithm.[9,15] The modifications concentrate on accelerating wave propagation to accelerate the convergence in pseudotime. A more detailed description can be found in Ref. 11.

Boundary Conditions

The boundary conditions affect the convergence, as well as the accuracy, of the numerical method. For transonic flow calculations, the far-field boundary conditions play a dominant role in convergence. The characteristic boundary conditions using the Riemann invariant are enforced for the subsonic inflow or outflow. Supersonic inflow is fixed to the freestream values and outflow is extrapolated from the values at the interior cells. The flow is tangent to the wall. At the solid wall, density and energy are extrapolated from the interior cells. The boundary conditions are also applied for each coarse grid.

Results and Discussion

To verify the present unsteady method, computations are made with basic finner configurations. The basic finner in Fig. 1 has been selected as a standard research configuration for validation purposes. The finner has a sharp nose and four wedge-shaped fins. To perform a grid refinement study, three sets of grid systems, which are displayed in Table 1, are generated using KGRID.[17] The body grid,

Table 1 Used grid systems for the basic finner

Grid	Body	Base	Fin tip
1	$105 \times 65 \times 49$	$17 \times 129 \times 17$	$25 \times 18 \times 25$
2	$105 \times 129 \times 73$	$17 \times 157 \times 25$	$25 \times 18 \times 25$
3	$209 \times 129 \times 49$	$33 \times 159 \times 17$	$49 \times 18 \times 25$

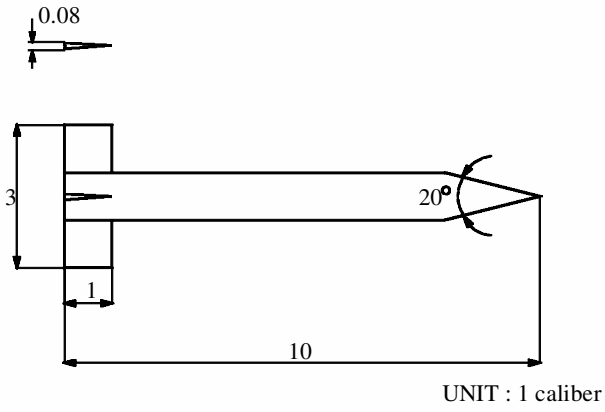

Fig. 1 Basic finner model.

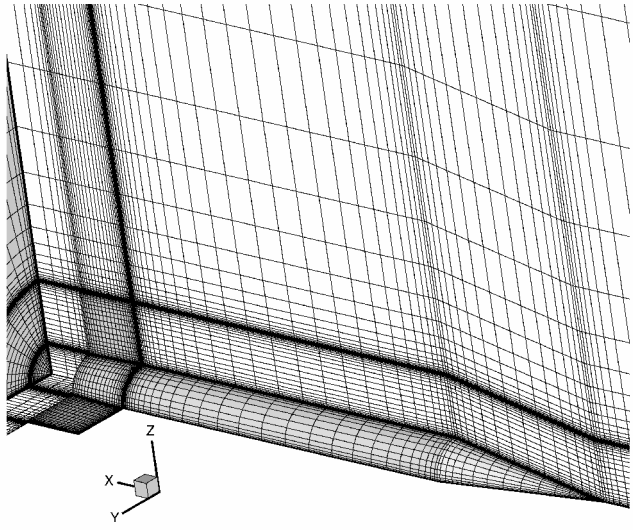

Fig. 2 Computational grid (grid 1).

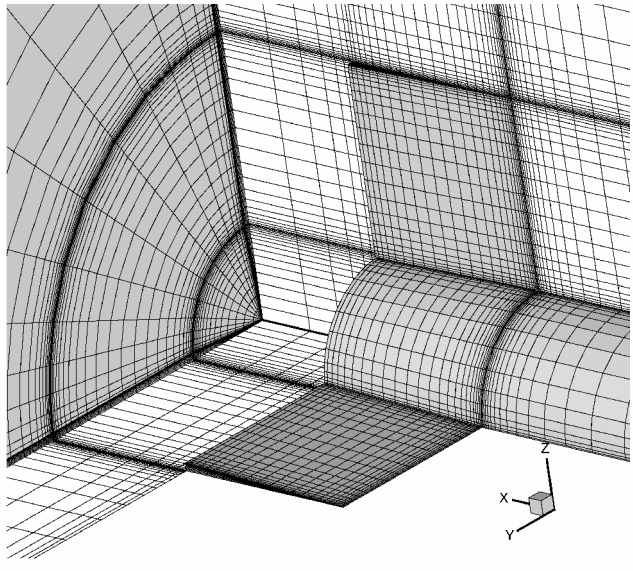

Fig. 3 Close-up view of grid 1 around fins and surface.

which is displayed in Fig. 2, consists of 105 node points in the axial direction and 65 and 49 points in the circumferential and radial directions, respectively. The grids are clustered normal to the surfaces in each direction. All computational grids have the corresponding grids for the base region. Figure 3 shows a close-up view of the surface grid around the rear body. Additional grids that enclose regions from each fin tip to the far field are included without any geometric approximations to the actual geometry. To examine the effect

of geometric approximations to the fin-tip geometry, a second grid system is employed. The second grid system eliminates the need for a fin-tip grid by modifying the fin-tip geometry, as shown in Fig. 4. An additional grid is included in the base region behind each of the fins. This merged grid has nearly the same grid resolution as grid 1 when compared to the grid for the actual geometry.

Grid refinement studies show that the largest variation is less than 3% variation for the computed pitch-damping moment coefficients. The variation between grids 1 and 3 is larger than that between grids 1 and 2. For the roll-damping moment coefficients, the largest variation is found between grids 1 and 2 rather than between grids 1 and 3. There is also less than 1% variation, except for the coefficient for a Mach number of 1.2, at which the variation is about 3.5%. Note that grid 2 is made by doubling the number of grid points for grid 1 in the circumferential direction and for the fin surface grids in the radial direction. The difference between grids 1 and 2 will be displayed in later. Unless otherwise stated, all results are for grid 1.

For all unsteady calculations, an initial solution is first obtained by solving the steady flow at the mean angle of attack and freestream conditions. The multigrid DADI algorithm is applied and converged to at least 10^{-4} for the L2-norm of density, which is normalized by the norm obtained after the first iteration. At each physical time step, the solution is marched in pseudotime until the normalized L2-norm of density reaches 10^{-2}. When the multigrid algorithm is used, it is found that the number of multigrid cycles for a physical time step is around 10 for the pitching motion and 5 for the rolling motion.

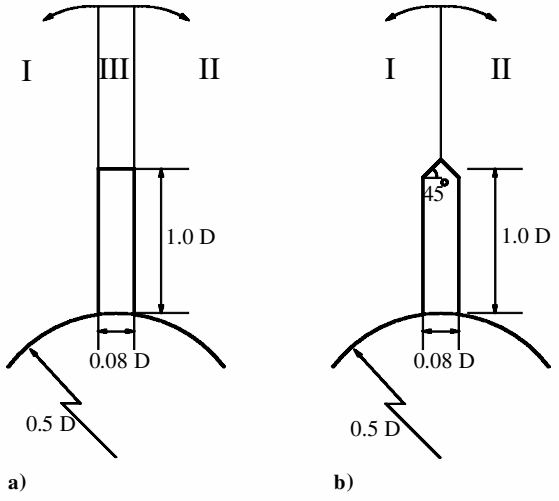

Fig. 4 Topologies for a) actual and b) approximated grids.

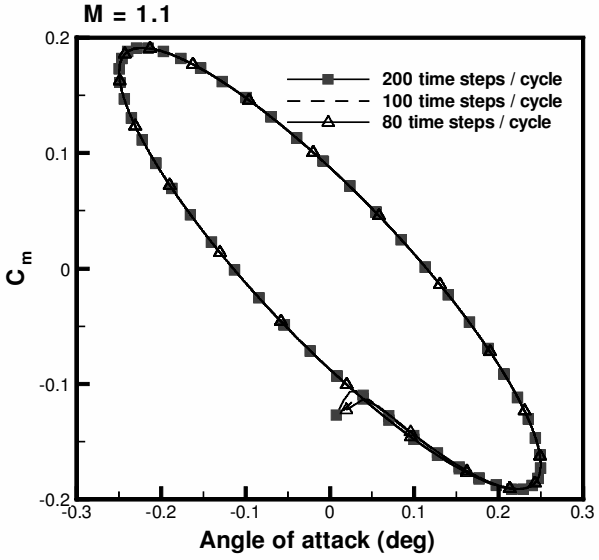

Fig. 5 Hysteresis loop of pitch-damping moment with time steps per cycle of motion at $M_\infty = 1.1$.

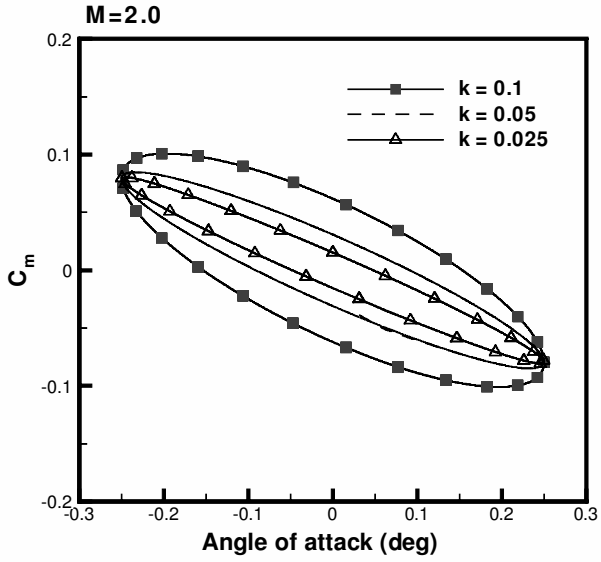

Fig. 6 Hysteresis loop of pitch-damping moment with reduced frequency.

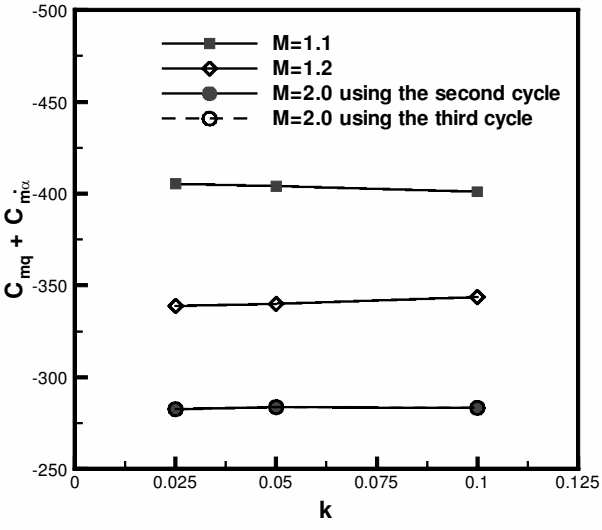

Fig. 7 Linearity of pitch-damping moment with reduced frequency.

Figure 5 presents the hysteresis loops for the pitch-damping moments of the unsteady simulations for the inviscid flows at zero mean angle of attack. In all cases, the amplitude of oscillation α_o is set to 0.25 deg. The inviscid assumption is reasonable because the small amplitude at zero mean angle of attack generates little flow separation in the flow direction. Displayed are three cycle loops for each time step. The computed moments on the second cycle are not different from the moments on the third cycle for this case. If the tolerance of convergence for the unsteady computations is not sufficient, the converged loops cannot be obtained within two or three cycles. Unless otherwise stated, the pitch-damping moment coefficients are calculated using 100 time steps per cycle of motion and the computed moments on the third cycle. The hysteresis loops of pitch-damping moments shown in Fig. 6 indicate that the generated damping moments due to the pitching motion increase with pitch rate. In turn, Fig. 7 shows that the pitch-damping moment coefficients are nearly constant for reduced frequencies of 0.025, 0.05, and 0.1. The coefficients at Mach 2.0 are the same magnitude when the integrations in Eq. (4) are performed by using the second and the third cycles. The linearity has also been shown in the numerical prediction[4] for a steady coning motion.

A comparison of pitch-damping moment coefficients with Mach numbers is displayed in Fig. 8. The experimental data and theoretical prediction are obtained from Ref. 14. No experimental data for

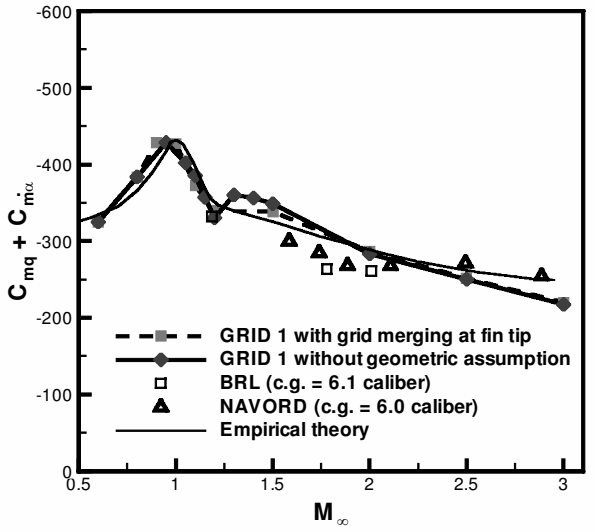

Fig. 8 Variations of pitch-damping moment coefficients with different geometries at various Mach numbers.

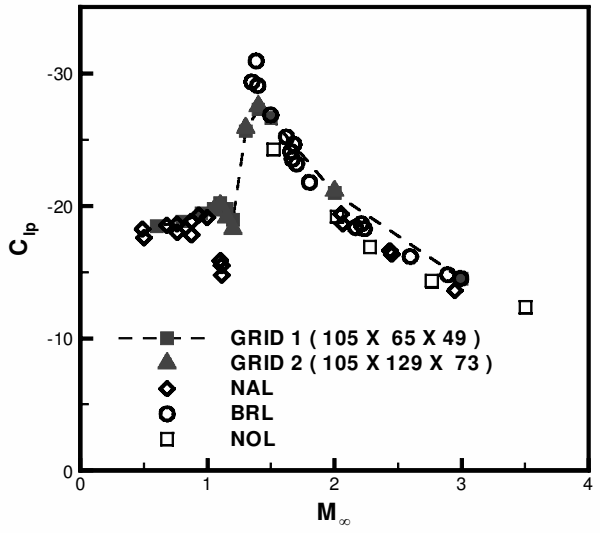

Fig. 10 Variation of roll-damping moment coefficient with grid resolution at various Mach numbers.

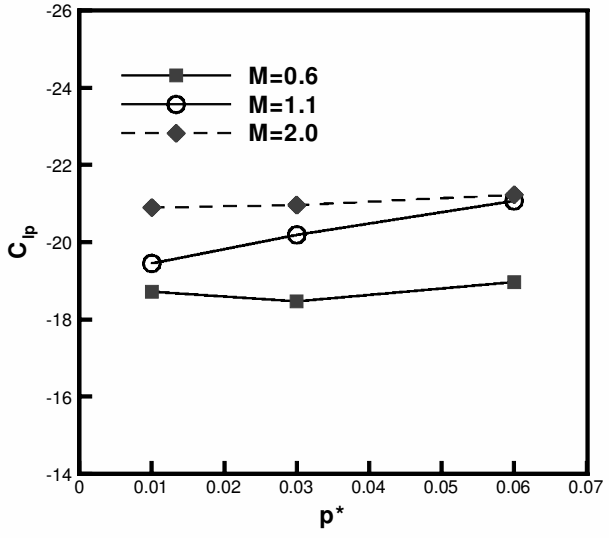

Fig. 9 Variation of roll-damping moment coefficient with roll rate.

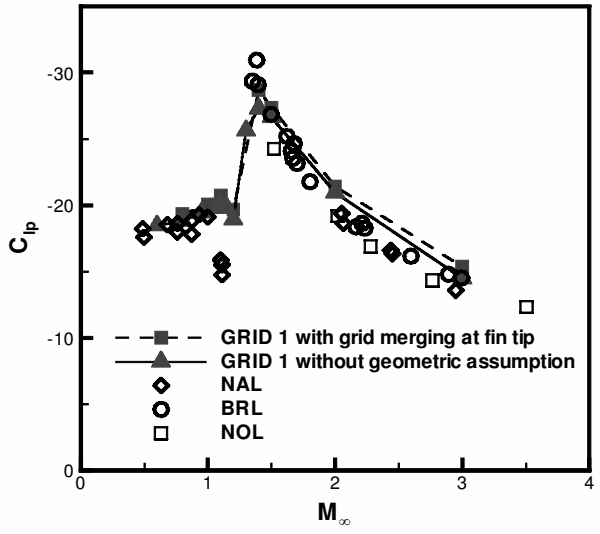

Fig. 11 Variation of roll-damping moment coefficient with geometry at various Mach numbers.

subsonic flows are found in any of the literature. For all computations, the c.g. is located at 6.0 caliber from the nose, and the reduced frequency is set to 0.05. The computed coefficients are in reasonable agreement with the experiment throughout all selected Mach numbers. A large variation that is observed in the transonic region shows that the basic finner has large pitch damping in the transonic regime. As shown, the geometric approximation near the fin tip produces some small differences at high transonic and low supersonic velocities. This peculiar behavior of the pitch-damping coefficients is shown for all applicable grid systems. The causal explanation is difficult, though it is possible. It is believed that the behavior is strongly related to an effect of shock interference generated by the fins. A similar effect for roll-damping coefficients will be discussed in a later paragraph.

The roll-damping moment is produced by the lift on the fins induced by the rolling motion. Murthy[13] performed experiments for roll-damping moment coefficients and discussed that the measured C_{l_p} was invariant with roll rate at subsonic and supersonic speeds. His experiments showed a large increase, followed by an equally large decrease, at about $M_\infty = 1.1$. The baseline roll-damping computations have been obtained with a constant roll rate p^* of 0.03, with a counterclockwise rotation when viewed from the rear. The variations of the roll-damping moment coefficient with roll rate in Fig. 9 show that the roll-damping coefficients are nearly the same for the computed subsonic and supersonic flows. In the case of M_∞ of 1.1, the magnitudes of the coefficients increase slightly with roll rate for all applied grids.

The computed roll-damping moment coefficients are compared with the experimental data for selected Mach numbers. Because the present calculations are performed under the inviscid assumption, the contribution of shear stresses at the wall to the coefficients is neglected. The computed results for both grids 1 and 2 displayed in Fig. 10 show good agreement with the experimental data, though they are slightly larger in magnitude than the experimental data at high Mach numbers. The largest variation of the roll-damping moments for the grid systems employed is found near $M_\infty = 1.2$. Figure 11 shows that the variation between the grids with different geometries is somewhat larger than that between the grids with different grid resolution, especially in the supersonic regime. Both results display a dip between Mach numbers of 1.1 and 1.2, though this dip is weaker than that of the experimental data. The dip results from the normal shock wave because the damping moment decreases immediately after the normal shock wave generates between the fins.

The present computations provide an explanation for the large increase immediately followed by the dip. Figure 12 displays the pressure distributions near the fins for various Mach numbers when grid 2 is employed. Because the finner rotates with a counterclockwise spin, the region of high pressure is produced at a lower fin surface. Subsequently, the roll-damping moment is produced by the

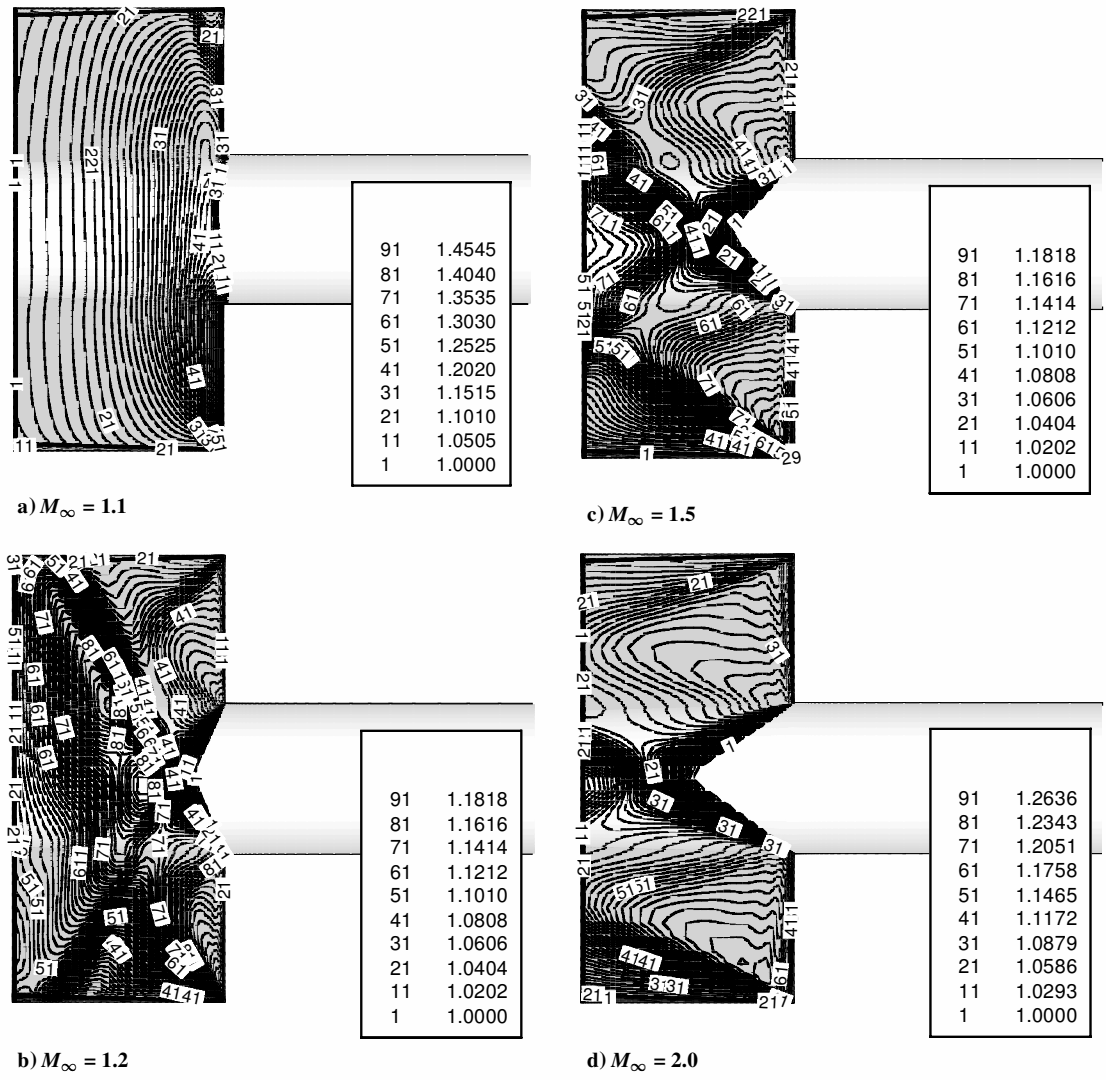

Fig. 12 Normalized pressure distributions near fins.

difference in pressure between the fins. The distributions show a transition from a normal shock to an oblique shock. A normal shock is generated at about $M_\infty = 1.1$. It then changes rapidly to an oblique shock as the Mach number increases. Finally, interference between the oblique shocks and the fins mostly disappears when the Mach number is higher than about 1.4. This means that a large increase in roll damping is caused by this interference. The roll damping steadily decreases as the Mach number increases after the interference disappears.

Conclusions

It was first argued that unsteady simulations can be used to predict damping coefficients without any constraints on the inertial coordinates. A dual-time stepping algorithm, combined with a multigrid DADI method, was applied to solve the unsteady Euler equations. The results using the Euler equations were in good agreement with the empirical and experimental data for the basic finner. The small dips that result from the normal shock generated between the fins were found for the pitch- and the roll-damping coefficients. The observation for the pressure distributions at Mach numbers above 1.1 shows that the transition of the normal shock to the oblique shock induces the large increase, followed by the dip for the roll-damping moment coefficients.

Acknowledgment

The authors gratefully acknowledge P. Weinacht for helpful suggestions.

References

[1] Sturek, W. B., Nietubicz, C. J., Sahu, J., and Weinacht, P., "Applications of Computational Fluid Dynamics to the Aerodynamics of Army Projectiles," *Journal of Spacecraft and Rockets*, Vol. 31, No. 2, 1994, pp. 186–199.

[2] Dillenius, M. F. E., Lesieutre, D. J., Hegedus, M. C., Perkins, S. C., Jr., Love, J. F., and Lesieutre, T. O., "Engineering-, Intermediate-, and High-Level Aerodynamic Prediction Methods and Applications," *Journal of Spacecraft and Rockets*, Vol. 36, No. 5, 1999, pp. 609–620.

[3] Tobak, M., Schiff, L. B., and Peterson, V. L., "Aerodynamics of Bodies of Revolution in Coning Motion," *AIAA Journal*, Vol. 7, No. 1, 1969, pp. 95–99.

[4] Schiff, L. B., "Nonlinear Aerodynamics of Bodies in Coning Motion," *AIAA Journal*, Vol. 10, No. 11, 1972, pp. 1517–1522.

[5] Weinacht, P., and Sturek, W. B., "Navier–Stokes Predictions of Pitch-Damping for Finned Projectiles Using Steady Coning Motion," *Proceedings of the AIAA 8th Applied Aerodynamics Conference*, AIAA, Washington, DC, 1990, pp. 632–642.

[6] Weinacht, P., Sturek, W. B., and Schiff, L. B., "Navier–Stokes Predictions of Pitch Damping for Axisymmetric Projectiles," *Journal of Spacecraft and Rockets*, Vol. 34, No. 6, 1997, pp. 753–761.

[7] Weinacht, P., and Sturek, W. B., "Computation of the Roll Characteristics of a Finned Projectile," *Journal of Spacecraft and Rockets*, Vol. 33, No. 6, 1996, pp. 769–775.

[8] Pechier, M., Guillen, P., and Cayzac, R., "Magnus Effect over Finned Projectiles," *Journal of Spacecraft and Rockets*, Vol. 38, No. 4, 2001, pp. 542–549.

[9] Jameson, A., "Time Dependent Calculations Using Multigrid with Applications to Unsteady Flows past Airfoils and Wings," AIAA Paper 91-1596, June 1991.

[10] Dubuc, L., Cantariti, F., Woodgate, M., Gribben, B., Badcock, K. J., and Richards, B. E., "Solution of the Unsteady Euler Equations Using an Implicit Dual-Time Method," *AIAA Journal*, Vol. 36, No. 8, 1998, pp. 1417–1424.

[11] Sung, C. H., Park, S. H., and Kwon, J. H., "Multigrid Diagonalized ADI Method for Compressible Flows," AIAA Paper 2001-2556, June 2001.

[12] Morrison, A. M., and Ingram, C. W., "Stability Coefficients of a Missile at Angles of Attack," *Journal of Spacecraft and Rockets*, Vol. 13, No. 5, 1976, pp. 318–319.

[13] Murthy, H. S., "Subsonic and Transonic Roll Damping Measurements on Basic Finner," *Journal of Spacecraft and Rockets*, Vol. 19, No. 1, 1982, pp. 86, 87.

[14] Moore, F. G., and Swanson, R. C., Jr., "Dynamic Derivatives for Missile Configurations to Mach Number Three," *Journal of Spacecraft and Rockets*, Vol. 15, No. 2, 1978, pp. 65, 66.

[15] Park, T. S., and Kwon, J. H., "An Improved Multistage Time Stepping for Second-Order Upwind TVD Schemes," *Computers and Fluids*, Vol. 25, No. 7, 1996, pp. 629–645.

[16] Pulliam, T. H., and Chaussee, D. S., "A Diagonal Form of an Implicit Approximate-Factorization Algorithm," *Journal of Computational Physics*, Vol. 39, Feb. 1981, pp. 347–363.

[17] Kim, Y., and Kwon, J. H., "KGRID: An Interactive 3D Grid Generator with GUI," edited by X. Hanxin, *Proceedings of The Fourth Asian Computational Fluid Dynamics Conference*, Univ. of Electronic Science and Technology of China Press, Chengdu, PRC, 2000, pp. 676–681.

P. Weinacht
Associate Editor